Ultrasonics 165 (2026) 108072

Contents lists available at ScienceDirect

Ultrasonics

journal homepage: www.elsevier.com/locate/ultras

Evaluation of ultrasonic transducer response and structural integrity using coded photoacoustic imaging

Linas Svilainis [a,*], Andrius Chaziachmetovas [a], Luca De Marchi [b]

[a] Electronics Engineering Department, Kaunas University of Technology, Kaunas LT-51368 Lithuania
[b] Department of Electrical, Electronic, and Information Engineering "Guglielmo Marconi", University of Bologna, Bologna, Italy

ARTICLE INFO

Keywords:
Laser ultrasound
Probe characterization
Transducer defects
Spread spectrum signals
Pulse compression

ABSTRACT

A novel technique for ultrasonic transducer photoacoustics imaging is presented. The technique is based on the analysis of the photoacoustic response of the light-absorbing layer placed on the transducer surface or, if the transducer layer or piezoelement absorbs light, directly on transducer surface. The focal spot of the pulsed laser is focused on the transducer surface, and the voltage generated on the output is used as a sensitivity metric at that location. Scanning in the *xy* plane produces a 2D sensitivity map. Use of pulsed laser diodes enables spread spectrum excitation which improves SNR and immunity to electromagnetic interference. A broadband photoacoustic response can be obtained with bandwidth limited by the antialiasing filter to 0.3–30 MHz. Experimentally evaluated lateral resolution for 50 ns pulse excitation was 148 μm or 203 μm depending on beam orientation. For 5–30 MHz chirp excitation after inverse filter PuC plus 0.2–25 MHz window resolution was 73 μm or 83 μm depending on beam orientation. The axial resolution in case of chirp excitation and pulse compression using inverse filter is down to 20 ns, which corresponds to 46 μm in PZT-5 ceramics or about 20 μm in PVDF or PVC. Signal decomposition into pulse positions allows for measuring the acoustic thickness of the transducer layers or resonant frequency of piezoelement. Capabilities are demonstrated on PZT transducers with a λ/4 matching layer and on PVDF strips array transducers.

1. Introduction

Laser ultrasound offers a broadband, non-contact method for injecting ultrasound waves into a test sample. A broad range of fundamental and applied research benefits from this phenomenon. Impressive imaging resolution can be achieved in biomedical imaging, and desired wave modes can be excited in non-destructive testing (NDT) applications. The application considered here is different: measurement of sensitivity map of ultrasonic transducers (air-coupled, immersion or contact) for the inspection of their response and structural integrity.

There is a variety and volume of commercially available transducers. Their quality is usually evaluated by the parameters (pulse shape, frequency spectrum, center frequency, relative bandwidth, sensitivity, impedance etc.) that are defined in standards [1–6]. However, transducers have a complex construction which can deteriorate over time, especially in the case of intense exploitation. Failure to spot transducer malfunctions can have serious consequences in biomedical or NDT applications [7–9]. Air-coupled transducers are especially complex and their active surface is fragile. Some procedures have been implemented for inspection [9–12]. In particular, the probe index, beam angle, physical state, sensitivity and pulse duration are to be evaluated [1]. Array probes can be inspected by monitoring the electrical impedance [13,14], acoustic directivity [1,10,15] or by comparing the phantom image to a reference [25]. Yet, the degree of severity, and damage nature cannot be addressed with these methods. Acoustic field, measured at some distance, can be reradiated backwards to the transducer surface using an acoustic holography approach [10,16,24], but such a procedure requires complex processing, can be subject to reverberation if the measurement plane is too close and the response from individual transducer layers still cannot be established. The approach of using reverberation [27] is simple, but does not provide information on layers, severity and location of the defects. Transducer tuning during development and production involves the application of several layers, contacts and backing [17–19]. The different layers are made of materials with specific values of acoustic impedance and attenuation [4,5], and their thickness is frequency-matched. The bonding between the layers, homogeneity of the layers, and their acoustic thickness accuracy are the factors affecting the final performance. Wrong layer attachment,

* Corresponding author.
E-mail address: linas.svilainis@ktu.lt (L. Svilainis).

https://doi.org/10.1016/j.ultras.2026.108072
Received 29 October 2025; Received in revised form 18 March 2026; Accepted 22 March 2026
Available online 23 March 2026

thickness deviation, and delamination can result in severe performance degradation [20]. The usage of metamaterials in air-coupled transducers can improve transduction efficiency [21–23], but these structures are tiny and fragile. Damage occurring on a metamaterial cell can degrade its performance locally. If a convenient inspection technique is available at each intermediate step, correcting measures can be applied or further assembly can be aborted, saving labor cost and materials of succeeding steps. Therefore, it is desirable to have a technique that indicates how individual segments of the transducer are performing in every assembly step. Also, a more quantitative procedure is desired for routine inspections, especially array probes [8,10,11]. Surface laser vibrometry scan [26] can be used, but this requires specific laser instrumentation, which is complex to operate and expensive.

In [28,29], a surface sensitivity map was proposed for transducer inspection. In particular, immersion scanning using a high-frequency focused transducer is used in [28] to obtain the sensitivity map. However, the resolution is limited to 400 μm with a 6 mm aperture, 25 MHz probing beam. Resolution improvement by increasing the aperture is limited by acoustic lens construction and critical angle; switching to higher frequencies (acoustic microscopy) would require more complicated equipment. Also, immersion measurements are not always allowed, for instance, when: i) the transducer is air-coupled; ii) the transducer is in the middle of an assembly procedure; or iii) a layer exposed is made of a material with wetting prohibited (e.g. soft outer matching layers of air-coupled transducer [17,18], hygroscopic glue, or uncured matching layers). An air-coupled scan using a second focused transducer is used in [29]. The signal received by the tested transducer is used to build a sensitivity map. With this method, a similar resolution (500 μm) can be obtained with a 20 mm aperture, 1 MHz probing beam due to shorter wavelength in air. Both techniques provide a local surface response as a map. Local disbonds or thickness variations are easy to spot from the sensitivity loss or the signal spectral analysis (conversely, this is not possible if the transducer's performance is evaluated by analyzing static capacitance, pulse shape, or frequency response measurements). However, the resolution of such an inspection is limited by the size of the focused beam. It is important that the bandwidth of the probing transducer matches, or preferably is broader than, the one being inspected.

The approach proposed here is based on photoacoustics [30]. The optical beam spot of the pulsed laser is focused on the transducer surface to produce a thermoelastic response and the acquired voltage on transducer output is used as sensitivity metrics at that spot. With this technique, the obtained beam spot is smaller than the focused transducer spot, improving the resolution. The size of the photoacoustic source is not affected by the transducer surface material. If the power density is kept within thermoelastic mode [31] ($<10^7$ W/cm^2), then the acoustic transduction is stable in time, and no damage to the transducer surface occurs. The transduction does not depend on acoustic impedance; therefore, a high-resolution and wideband acoustic signal source is obtained. In our approach, pulsed laser diodes are proposed for excitation. These devices are available at 10 W to 600 W pulse power [33] (or more in overdriving [32]) as commercial, relatively low-cost components. Pulse durations in the range of 10 ns to 1000 ns can be used, which matches the range of 0.5–50 MHz for conventional ultrasonic transducers. It is worth noting that the efficiency can be improved by using a spread spectrum signal excitation [41–43]. If Arbitrary Position and Width Pulse (APWP) sequences [34] are used, the excitation spectral content can be programmed [35,36] to match the required shape. The laser drivers capable of APWP or coded sequences excitation are not currently available commercially, but the development of such a laser driver has been reported in [34]. A similar driver was used here. Broadband photoacoustic responses can be obtained if only the pressure signal registered on the front-facing piezoelement electrode is used.

The inspection results of two ultrasonic transducer types are presented to demonstrate the performance of the proposed solution.

2. Materials and methods

The proposed inspection approach is based on focusing a laser beam on the surface of an ultrasonic transducer. The photoacoustic response is creating a voltage signal on the transducer output, which serves as a sensitivity metric at the location where the laser beam was hitting the surface. A 2D sensitivity map can be produced by scanning the beam over the whole surface. The waveform of the photoacoustic response to the laser pulse can be analyzed to distinguish the different components corresponding to the different elements of the transducer construction layers. The time of flight (ToF) of these pulses can be used to calculate the acoustic thickness of layers constituting the transducer.

2.1. Transducers used in the inspection experiments

Two types of transducers were investigated: i) a standard PZT-based transducer with λ/4 matching layer attached; ii) an air-coupled transducer based on an array of PVDF films [23]. In particular, the first transducer type is a 10 mm in diameter and 1 mm thick piezoceramic disk (Fig. 1) made form PIC155 material (Physik Instrumente GmbH, Germany). This transducer type represents the most common construction [17–19].

The piezo-disk has 10 μm thick screen-printed silver electrodes on both sides, one serving as signal, another as ground. The ground electrode also has a tab on the opposite side so electrical connections can be made from a single side. Its properties are: longitudinal piezoelectric coefficient $d33$ equal to −180 pC/N (approximately corresponding to Navy II PZT), density equal to 7800 kg/m^3, resonance frequency equal to 2.25 MHz. The transducer was investigated at several assembly stages: i) only PZT disk, ii) PZT disk with part of electrode missing, iii) PZT disk with matching layer attached and iv) PZT disk with segment of matching layer attached. It is worth noting that the transducer at these assembly stages cannot be immersed in water, therefore measurements done using the laser excitation are especially attractive. The matching layer was attached to the disk to demonstrate what measurements can be made at the different assembly stages.

The second transducer type used an array of vertical strips (Fig. 2) made from 50 μm thick uniaxially stretched PVDF film sheet with 100 nm thick sputtered aluminum electrodes (PolyK LLC, US). It is an air-coupled transducer, proposed in [23].

The strips were cut 3 mm wide (along the d_{31} direction) and 20 mm long (along d_{32}). The PVDF film was characterized by the following parameters: $d_{33} = 23$ pC/N, $d_{31} = 30$ pC/N and a very low d_{32}. Strips were placed into a stack with 150 μm thick conductive spacers at the ends (390103, Würth Elektronik GmbH, Germany) with the same polarity electrodes facing each other. This is an air-coupled transducer; consequently, immersion is prohibited even in the final assembly case. Measurements with focused air-coupled transducer would not reveal individual strips, since these are placed at 200 μm pitch and 1 MHz transducer with 20 mm aperture will provide only 500 μm focal spot in the best case. Therefore, measurements using laser excitation are the

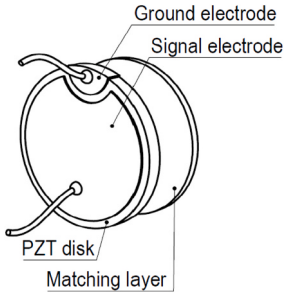

Fig. 1. First type PZT-based transducer with λ/4 matching: exploded view of transducer construction.

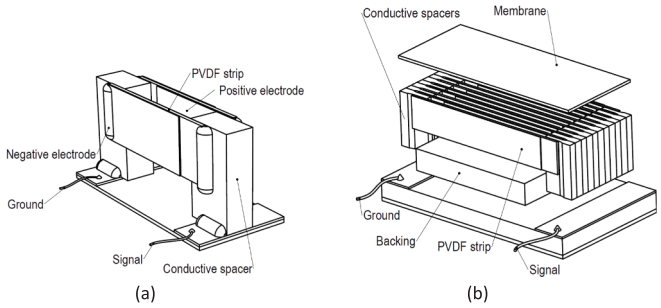

Fig. 2. Second type PVDF-array transducer: intermediate assembly stage (a), and exploded view of final construction (b).

only viable option in this case. Such a transducer was investigated at several assembly stages: first, we inspected just a pair of PVDF strips suspended in air (Fig. 2a, stage 1). Then, the transducer was backed by adding 4 mm of UV-curable plastic poured on 1.5 mm FR4 plate (stage 2). Subsequently, it was covered by a membrane (stage 3), and, finally, a larger PVDF strips array, backed and covered by the membrane, (stage 4), i.e. the whole device as depicted in Fig. 2b.

2.2. Measurement setup

The full setup used for data acquisition is presented in Fig. 3.

A dedicated data acquisition system, designed and manufactured by Kaunas University of Technology [40], was used. The system has a 3D positioning scanner with 10 μm step resolution, programmable gain preamplifiers, and 100 MHz sampling frequency. The clock frequency is used for synchronizing the transmission and acquisition channels. The maximum sequence code length for the production of APWP waveforms is equal to 16 ksamples. The acquisition system features two synchronous, 10-bit 32 ksamples deep channels. Channel 1 was used to collect the transducer output signal after a 47 dB preamplifier. The preamplifier input impedance is equal to 1 kΩ. A third-order Butterworth filter was used as an antialiasing filter at the output. For the PZT transducer, its bandwidth was limited to 0.3–30 MHz. For the case of the PVDF transducer, the bandwidth was set in the 0.1–3 MHz range. Channel 2 was used to collect the laser current monitor output signal.

An edge-emitting 905 nm semiconductor laser diode SPL UL90AT08 (OSRAM Opto Semiconductors GmbH, Germany) was used thermoelastic excitation. The diode sustains a 120 W peak power at maximum 40 A drive current. The emission aperture is 220x10 μm. The laser driver is based on an NVTFS6H888N MOSFET (ON Semiconductor, USA) with source current feedback topology. More details on this topology can be found in [37]. The lens system (355397-B and 355230-B, Thorlabs, Inc., US) produced 2:1 beam size reduction, and was mounted in a 3D-printed holder together with the driver PCB (Fig. 4).

The laser driver can deliver arbitrary position and width pulse (APWP) sequences, where individual pulse duration and gap between pulses can vary between 20 ns to 1000 ns, with a pulse current programmable up to 40 A. Shorter pulse durations can be used, but more distorted pulses are generated in such a case. The total sequence length is limited by the driver's thermal drift, for example, the maximum

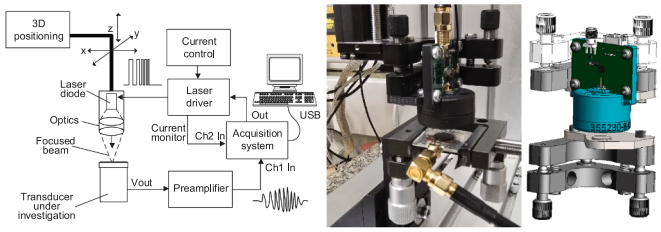

Fig. 3. Data acquisition setup for transducer sensitivity map measurement.

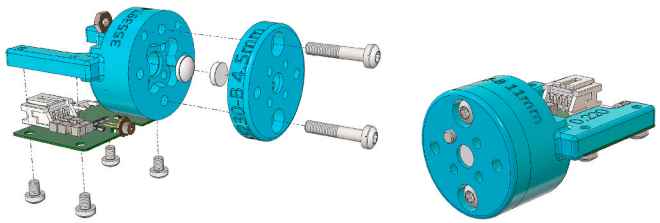

Fig. 4. Laser source construction.

sequence duration without distortion is equal to 2 μs at 40 A, up to 10 μs at 10 A and so on. In the experimental measurements presented in the following section, for the single-pulse case, a 20 A peak current was used (corresponding to a 68 W peak according to the datasheet), while, for the spread-spectrum excitation case, a 1 μs long pulse sequence at 10 A peak current was used (corresponding to 34 W peak).

The measured laser beam profile is presented in Fig. 5.

From Fig. 5, it can be noted that the beam profile is asymmetrical: at the −6 dB level, the beam size is 103x7 μm. This is a typical characteristic of edge-emitting laser diodes. Such asymmetry turned out useful in this investigation: along the wider dimension, the beam can be used for quick localization of regions of interest and, if higher resolution is required, the beam can be rotated 90° to provide 7 μm resolution. A good example is PVDF strip edge. The strip is 50 μm thick, so the 103 μm resolution is suitable for strip position location. Then, once the center position of the PVDF strip is found, scan can be carried out with 7 μm resolution.

The maximum laser fluence, assuming a 68 W peak power, is $0.94 \cdot 10^{-7}$ W/cm^2, less than the upper limit for thermoelastic excitation [31]. The actual fluence will be even lower due to the alignment and optical system losses.

A constrained (buried) [32,33] laser ultrasound source was used (sometimes addressed as fourth regime in laser ultrasound). Most acoustic matching materials, used in transducer design, are dark and polymeric. Then, most of the laser beam is absorbed in the bulk of material, polymeric material thermal expansion coefficient is large (e.g. PVDF is [62], ABS is 140 μm/m·K vs. 23 μm/m·K for aluminum), i.e. high efficiency constrained source is produced.

The edge of PVDF strip, which was used in the second type of inspected transducer (refer Fig. 2), is open (no metal electrodes). Therefore, PVDF material is directly exposed to laser radiation. Unfortunately, PVDF is almost transparent for 905 nm laser light, absorption is less than 1%, much smaller than dark, opaque plastic. But, if laser beam (7 μm size) hits the edge of the strip (50 μm thick), laser beam can propagate into PVDF. Aluminum coating serves as reflector, creating ideal waveguide. The beam is trapped and fills the thickness. Laser beam interaction with PVDF is over its entire height (3 mm), heating approximately 100 μm x 50 μm x 3000 μm volume. Furthermore, part of beam can be reflected from PVDF-air interface at the opposite end, creating multiple propagation path, which increases beam interaction with PVDF. Thermal expansion coefficient of PVDF is 100 μm/m·K [62]. Once heated over entire 3 mm height, 1 °C temperature increase can create 0.3 μm extension. This direction is aligned with d31 mode (which

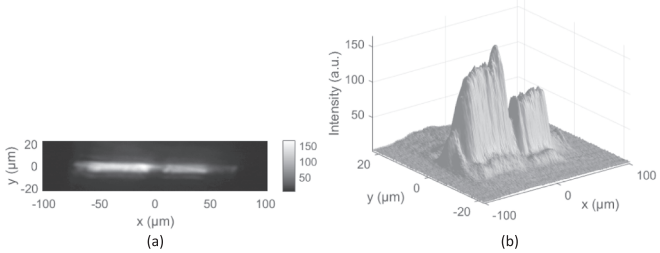

Fig. 5. Laser beam profile at focus.

is favored in this transducer design [23]), d_{31} coefficient is quite large so some voltage response can be expected.

Yet, if piezoelement is inspected perpendicular to electrode, silver or aluminum have large reflectivity and laser energy absorption is low, around 1% for Ag, 15% for Al according to [61]. Skin depth for silver is small, 20–30 nm, e.g. thermoelastic expansion is very weak and on surface only. Such source does not have directivity normal to the surface because majority of expansion is along the surface. In such a case, an absorbing layer was applied to increase absorption and create a constrained source with directivity normal to the surface [37–39]. Two types of absorbing layer were experimented: i) spray-coating with a black paint (BOKSC263206 type from Bostik SA, Colombes, France, 800 C°) and ii) black 150 μm thick PVC tape (1905B, MULTICOMPpro, PRC). The presence of such a layer improves the acoustic pressure produced, due to improved energy absorption and it also reduces the amplitude of the surface wave [33,38,39].

Two types of excitation signals were used: i) single pulse, duration 30 ns, 50 ns, 100 ns or 200 ns and ii) rectangular unipolar spread spectrum signal (linear frequency modulation, LFM or chirp) 1 μs long, with bandwidth 2–20 MHz, 5–25 MHz, 5–30 MHz and 3–30 MHz.

Spread spectrum excitation offer several advantages: i) SNR can be improved, ii) broader spectral coverage can be achieved [41–43], iii) spectral content can be programmed to compensate the system losses [34–36] and iv) immunity against the electromagnetic interference (EMI) can be achieved. Spread-spectrum signals can be compressed using pulse compression (PuC) using matched filter (cross-correlation) [41,42] or inverse filter proposed in [43]. While single pulse excitation is simple, easy to interpret, it is not immune against electromagnetic interference (EMI). EMI is produced by the PWM of motor drivers of the positioning system, by the switched-mode power supplies (SMPS), and by the computer. The EMI basically generates a HP-filtered spike from each front of rectangular PWM waveforms of SMPS or scanner motors, USB communication. These appear at random time positions of the acquired waveform and can be barely distinguished from the thermoelastic response to short laser pulses. Conversely, spread-spectrum signals have spectral components distributed in time. PuC compresses these components into single time instance. Placement of spectral components in time is different from chirp for noise and EMI, therefore PuC decorrelates then. Result is that chirp energy is concentrated, but EMI and noise energy is deconcentrated. In such case much higher EMI immunity and SNR can be obtained after PuC if spread-spectrum excitation is used. A narrow pulse can be expected after PuC (from 55 ns down to 35 ns, depending on the bandwidth coverage of the chirp) but with a much higher SNR and reduced EMI influence.

2.3. Signal processing

Data was processed off-line using MATLAB (2022b, MathWorks). The signal processing steps to get the desired sensitivity map are very simple in case of single-pulse excitation: gate position for the desired pulse in the acquired waveform needs to be selected, and, subsequently, either the peak- or RMS- values within the gate are used as sensitivity metrics. In the case of spread-spectrum signals excitation, the PuC should precede the gating operation.

PuC is performed in frequency domain. Laser current signal is used as reference for PuC filter derivation. Received signal $s_{RX}(t)$ and laser current signal $s_{Laser}(t)$ are transformed into frequency domain using DFT. For compression using matched filter (MF):

$$S_{\mathrm{MF}}(\omega) = S_{RX}(\omega)conj(S_{Laser}(\omega))W_{BP}(\omega) \tag{1}$$

where $S_{RX}(\omega)$ and $S_{Laser}(\omega)$ are received and laser signals in frequency domain, $S_{\mathrm{MF}}(\omega)$ is signal after matched filter in frequency domain. Filter $W_{BP}(\omega)$ is a Tukey window with tapering 0.5 (bandpass, BP, filter). The upper and lower passband frequency can be adjusted. Window is optional and is intended for near-range sidelobes suppression, producing a mismatched filter. Its type and shape can be different from used here, for instance based on the reactance transformation [63].

PuC using matched filter results in far-range correlation sidelobes [52,53] which are caused by Fresnel ripples of rectangular chirp excitation. PuC using the inverse filter possess same compression property as matched filter. But it has much lower sidelobes, because it deconvolves the excitation from received signal so Fresnel ripples of chirp are removed [43]:

$$S_{IF}(\omega) = W_{BP}(\omega)S_{RX}(\omega)/S_{Laser}(\omega). \tag{2}$$

Same as above, reference signal $S_{Laser}(\omega)$ is the excitation code or voltage, measured on transmitting transducer clamps. BP window $W(\omega)$ is not optional, in this case it is intended for noise gain reduction in low SNR regions and near-range sidelobes suppression. Response obtained after inverse filter PuC can be considered as one obtained after ideal delta pulse excitation but with improved SNR.

After PuC using (1) or (2) signal is transformed back into time domain using IDFT.

Processing for the estimation of the layer acoustic thickness involves waveform decomposition into multiple subcomponents (i.e. individual pulses), with the subsequent estimation of time of flight (ToF) and amplitude. Reiterative deconvolution, described in [44] was used for this procedure. Such a procedure requires a reference waveform with single pulse. But received signal contains several pulses due to reverberation inside upper layer or piezoelement thickness. Usually, it can be derived from a measured waveform by gating out the interfering pulses [49–51]. However, in application analyzed here signals sometimes overlap. This is hampering the isolation of the single-pulse response. To overcome this problem, the single-pulse response can be produced synthetically using a given response model [45–48]. A different approach was adopted here: the synthetic reference waveform was produced from the excitation signal passed through the derived system model: first, the system response model (8 zeros and 4 poles IIR filter) was trained on 30 ns pulse response (which has no overlapping), forcing the approximation of only the first pulse; then the system response model was applied to the rest of the excitation signals. The time delays of the extracted pulses, obtained by deconvolution, were sorted in ascending order and the ToF difference, depending on layers' construction, calculated. Finally, ToF difference was converted to a frequency ($\lambda/4$ if matching layer or $\lambda/2$ if thickness resonance).

3. Results and discussion

The inspection of the transducers was carried out with a multi-scale resolution approach: first, using relatively large, 400 μm steps in the XY scanning. In this phase, the regions with large photoacoustic response were located and single-point measurements were performed by averaging 100 waveforms for each scan point. These measurements were used for temporal response studies and single-pulse model derivation. In a second phase, data were collected using smaller, 100 μm steps in order to obtain 3D datasets. These datasets were used for spatial response studies and acoustic layer thickness measurement.

3.1. PZT element coated by black paint

In this experiment only PZT piezoelement, spray-coated using black paint, was inspected (Fig. 6). Laser beam, hitting the absorbing paint, produces point-like thermoelastic source. This creates longitudinal (marked as L-wave in drawing), surface skimming longitudinal (SSL-wave), shear (S-wave) and Rayleigh (R-wave) waves. SSL leaks into head wave. Only two response pulses, are of concern in this experiment, both are related to L-wave. One, named L1, is a positive pulse, produced on transducer clamps when L-wave hits the upper electrode (PZT polarization is assumed such that signal electrode is positive when element is compressed). Another (L2) is a negative pulse, produced when L-wave hits the lower electrode.

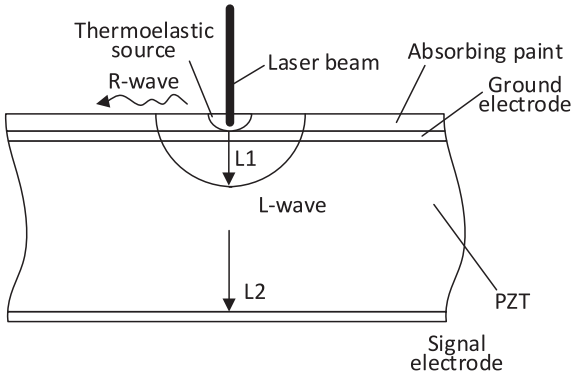

Fig. 6. PZT-based transducer construction with laser beam excitation setup and waves propagation explained.

A-scan of the voltage on the PZT element when excited by 20 A pulse is presented in Fig. 7a, b, c. The L1 pulse (starting at 0.2 μs) is generated when the photoacoustic pulse hits the closest PZT electrode. The L2 pulse (starting at 0.45 μs) is generated from interaction with the second electrode. The succeeding pulses are out of interest, these are generated by secondary reflections.

The black curves on Fig. 7d, e, f show the spectra of the received signal for L1 pulse only (signal is zeroed beyond the gate indicated by blue and red markers in Fig. 7a, b, c). The blue curves show the nominal AC response as can be expected from the nominal pulse duration (the one supplied to the input of laser driver). From the broadening of the actual spectrum, it can be inferred that the actual pulse duration is slightly shorter than the nominal pulse. Despite these slight differences, it can be concluded that duration of the response follows the excitation pulse. Sensitivity is always the same: 10 mV at 68 W laser power or approximately 150 μV/W. AC response is broadband and covers frequencies of interest (up to 30 MHz).

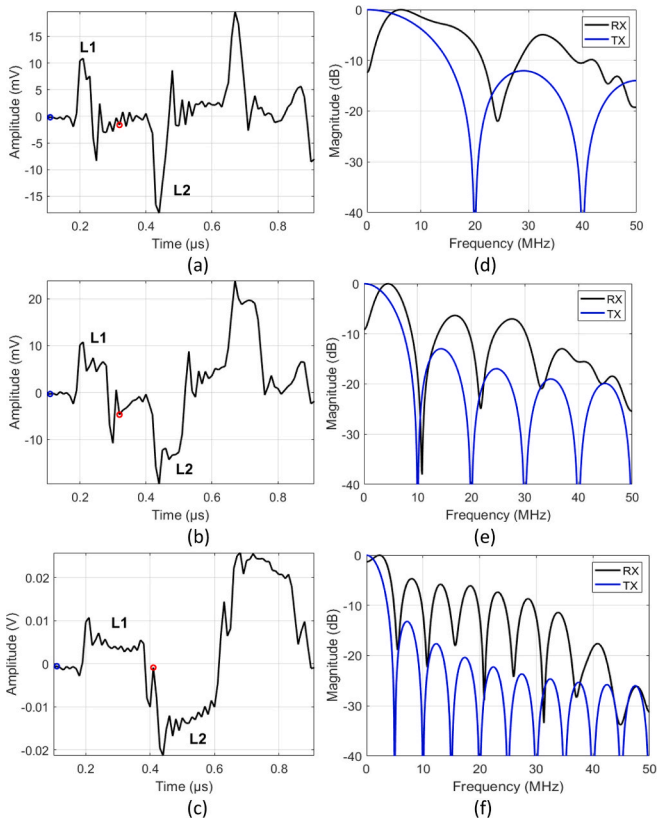

Fig. 7. Voltage on the PZT element (coated by black paint) when excited by pulses of different durations: 50 ns (a), 100 ns (b) and 200 ns (c). (d), (e) and (f): spectrum of L1 pulse (blue, red markers: gate), black – received signal, blue curves – excitation.

Laser current waveform, when laser is driven by 5–25 MHz 1 μs long 10 A chirp spread spectrum signal is plotted in Fig. 8a. The voltage received on PZT element clamps (Fig. 8b) was processed using PuC using i) matched filter with additional BP, ii) inverse filter with additional BP and iii) only inverse filter with no additional BP. Results of are presented in Fig. 9.

There are two reasons for high frequency ringing. One is a near-range sidelobes. Another is a reverberation in black paint layer. From 42 MHz peak (Fig. 9f) it can be assumed that paint thickness is approximately 26 μm. It can also be noted that the mainlobe after PuC is narrow, for filtered case it is 30 ns and 20 ns for unfiltered case. The frequency-domain response indicates better spectral coverage by chirp compared to the case of a single pulse excitation.

Pulse L1 in Fig. 7 appears exactly same time (0.2 μs) as current monitor pulse, meanwhile L1 in Fig. 10 is slightly shifted left. This shift appears due to PuC processing.

It can be concluded that the attainable bandwidth corresponds to the antialiasing filter AC response, 0.3–30 MHz, i.e. much broader than expected bandwidth of undamped PZT disk with thickness resonance of 2 MHz. The reason is that only L1 pulse (response from upper electrode) is analyzed. Broadband response allows to achieve high spatial resolution. The expected axial resolution then is 30 ns, which can correspond to 130 μm in PZT-5 ceramics or about 68 μm in PVDF or PVC. The application of the inverse filter allows to improve the axial resolution down to 20 ns, which corresponds to 46 μm in PZT-5 ceramics or about 20 μm in PVDF or PVC.

Next experiment was intended to evaluate the spatial response in case of electrode loss. A 50 μm wide and approximately 50 μm deep notch was laser-engraved on the top and bottom (Fig. 10), separating the left and right parts of the electrode. Right part electrodes were connected to receiving amplifier and left electrodes were left floating. The piezoelement was fitted into holder PCB and spray-coated using black paint.

B-scan over the 4 mm range across this cut was performed in such a way that the cut remains in the center (at $x = 0$). The B-scans of the photoacoustic response when excited by a 50 ns pulse (a), 200 ns pulse (b), 5–25 MHz chirp after PuC using matched filter plus 0.5–35 MHz window (c) and PuC using inverse filter plus 0.5–35 MHz window (d) are presented in Fig. 11.

Positive effects of PuC can be noted: resolution is improved compared to 50 ns pulse excitation. The artefacts generated by the matched filter-based PuC can be seen in Fig. 12c: there are far-range sidelobes that cyclic-wrap the tail into start of the signal (note the ghost lines at 45° angle). Inverse filter-based PuC (Fig. 10. d) have much smaller artefacts. The excitation using 200 ns is too long: many signals are overlapping.

Material of Fig. 12 is intended to explain the results of Fig. 11.

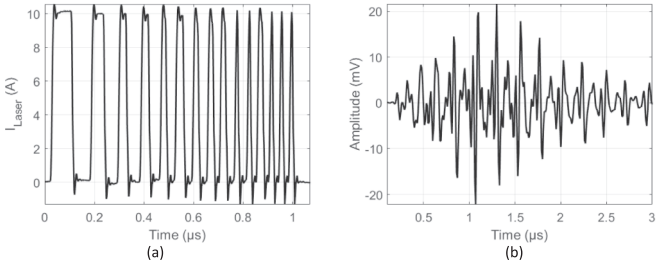

Fig. 8. Laser current for 5–25 MHz 1 μs long 10 A chirp (a) and signal registered on PZT element clamps when excited by 10 A 5–25 MHz 1 μs long chirp (b).

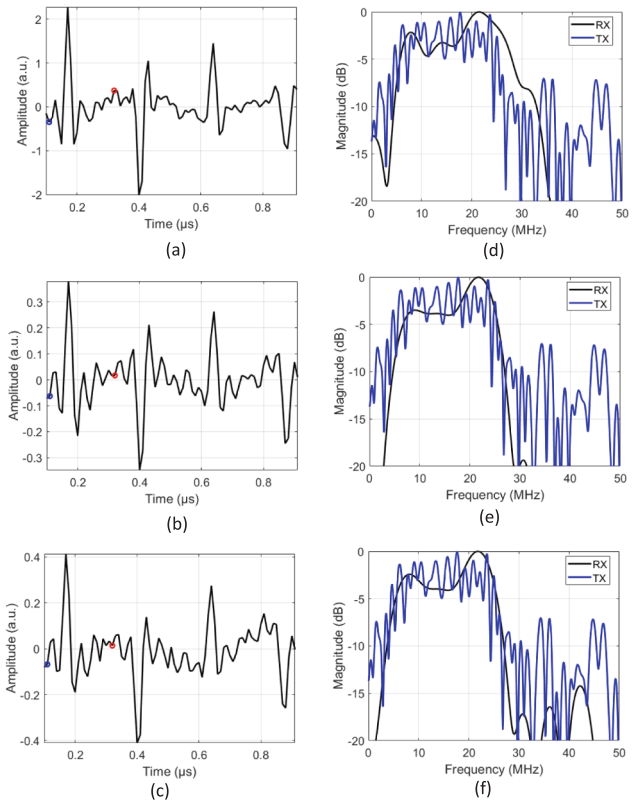

Fig. 9. Result of PuC applied on voltage received on PZT element (coated by black paint) when excited by 5–25 MHz 1 μs long chirp. (a)-(c): in time. (d)-(f): in frequency domain. (a),(d): inverse filter and 0.5–35 MHz window (top), (b), (e): matched filter and 0.5–35 MHz window and (c),(d): matched filter only. Black: received signal, blue: expected AC response according to code sequence used for excitation. Blue and red circles indicates the start and end of the time window for spectrum calculation.

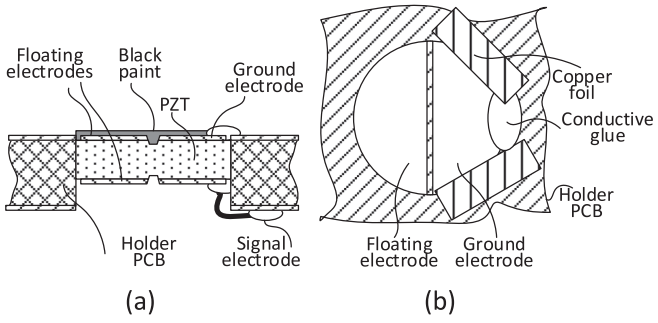

Fig. 10. PZT-based transducer with simulated loss of electrode: side (a) and top (b) view of construction.

When laser beam is positioned over the right (active) electrode, longitudinal, normal to the surface wave produces positive electrical pulse L1 when it hits the upper active electrode. Polarity is positive because PZT is in compression. Some faint L1 signal can be seen at negative x in Fig. 12b or Fig. 11. It is produced because of capacitive coupling between floating and active electrodes. L2 pulse is produced when same wave propagates over PZT thickness and hits lower electrode. Polarity is negative because PZT is in expansion. Part of pressure normal to the electrode contributes the most while laser beam is over active electrode. However, oblique part of L wavefront remains when laser beam is off the active electrode. It is registered as parabolic part of L2 at negative x in Fig. 11 or Fig. 12b. Note that L-wave wavefront (Fig. 12a) slightly deviates from spherical. The reason is PZT

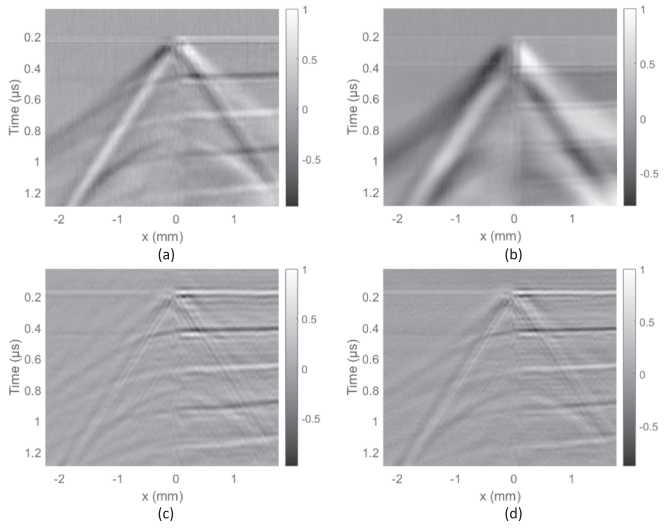

Fig. 11. B-scans of the PZT element with electrode loss when excited by a 50 ns pulse (a), 200 ns pulse (b), 5–25 MHz chirp after PuC using matched filter and 0.5–35 MHz window (c) PuC using inverse filter and 0.5–35 MHz window (d). Grey scale amplitude is in a.u.

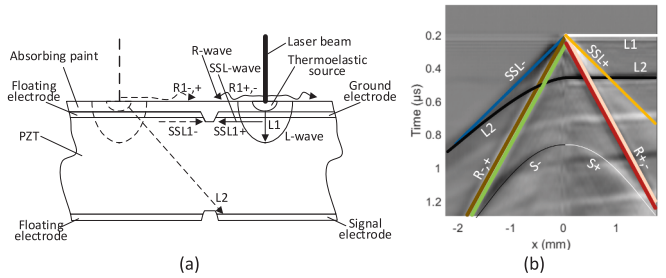

Fig. 12. Explanation of Fig. 12 results: topology and wave types (a) and B-scan with wave traces indicated (b).

polarization: propagation across the thickness (d33) is faster than along the surface (d31). Same anisotropy applies to S-wave, it does not have components normal to the surface and in order to convert to longitudinal needs to arrive at some angle. Therefore S-wave appears (S + and S- in Fig. 12b) at more than twice the distance between L2 and L1. It is not used in this investigation. SSL-wave can not be registered directly, because the net pressure exerted on upper electrode is always the same. But once SSL-wave leaves the electrode (laser beam is positioned over floating electrode), net pressure is changing and it can be registered (note the SSL + line in Fig. 12b). Front of SSL is outwards from PZT (expansion) so voltage produced while it is on electrode is negative. But once it goes off electrode, opposite sign is produced and SSL + is positive. Meanwhile situation with SSL- (note the dashed part of drawing in Fig. 12a) is opposite: it is registered when it reaches active electrode, therefore sign is negative. Similar situation is with R-wave, only, differently from SSL, more pressure is directed normal to the surface, it has a positive (outwards from PZT) front plus negative tail. Therefore right part of Fig. 11, Fig. 12b contains R+,- and left part has R-,+ response.

FEM simulation results are presented in Fig. 13.

Laser excitation was simulated by ideal 30 ns Gaussian pressure pulse produced by 100 μm wide boundary load. Notch penetration (refer Fig. 12) into PZT was not simulated, electrode was zero thickness with gap width 100 μm.

Similarity of the B-scan obtained by laser beam scanning (Fig. 13b) to Fig. 11a result allows to conclude that laser excitation can be considered as ideal pressure source acting normal to the surface.

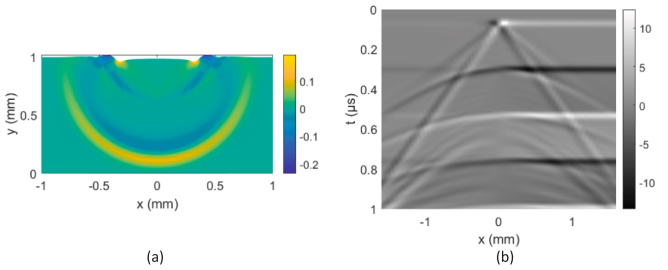

Fig. 13. FEM simulation results: propagation in PZT, stress and displacement (a), and B-scan obtained after beam scanning (b).

The absolute maximum value was extracted using the gate of L1 pulse (blue and red markers in Fig. 9) and C-scan images produced (refer Fig. 14). Images obtained can be considered as electrical activity indicators for upper electrode.

It can be noted that electrode loss can be detected, only PuC image provides higher contrast and resolution. Edges of the notch appear bright because of SSL and R-wave registered at this interface. Again, edges are narrower in case of PuC image. Matched filter based PuC provides more contrast because SNR is higher than inverse filter can provide. Round shape is missing on the right side (positive x) due to copper foil applied here for ground connection.

3.2. PZT element with black PVC tape on top

PZT element was fixed in PCB holder and covered by the black sticky PVC tape (Fig. 15a). PVC tape is 150 μm thick, much thicker than 26 μm thick paint coating. Use of thick PVC tape is offering advantage of deep-buried thermoelastic source. Interaction with laser beam is over larger area, source is larger in depth than in width. Therefore, more energy is directed normal to the surface. Refer Fig. 15 for this experiment details, drawings are not to scale for clarity.

Only longitudinal waves are registered in this experiment. Positive electrical pulse L1 is produced first when longitudinal wave produced in PVC layer hits the upper electrode. Polarity is positive because PZT is in compression. Some of signal entering PZT is reflected back to PVC,

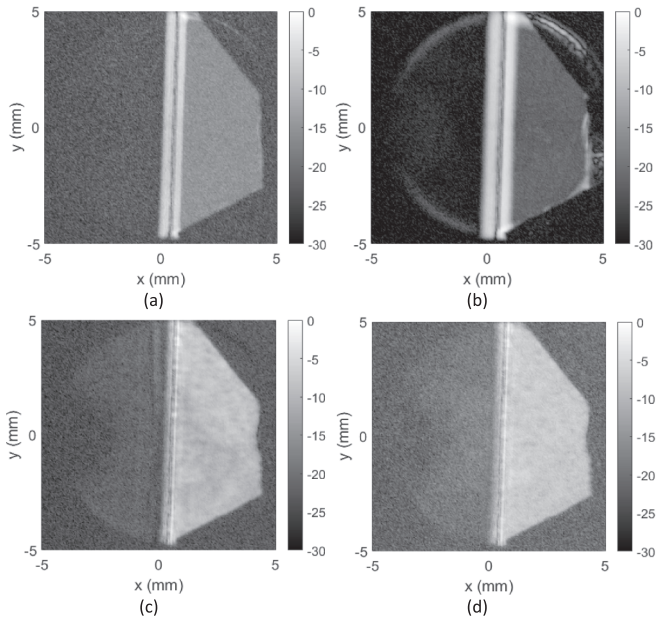

Fig. 14. C-scans of the PZT element with electrode loss when excited by a 50 ns (a), 200 ns pulse (b), 5–25 MHz chirp after PuC using matched filter 0.5–35 MHz window and (c) PuC using inverse filter 0.5–35 MHz window (d). Grey scale amplitude is in dB.

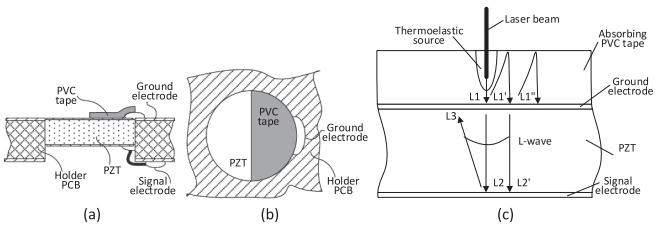

Fig. 15. PZT with black PVC tape as PZT matching layer: side view (a), top view (b) and explanation of waves generation (c).

reflected from PVC-air interface (polarity inversion) and registered on upper electrode again as L1′. Some of signal is again reflected back to PVC, reflected from PVC-air interface (polarity inversion) and registered on upper electrode again as L1″ and so on. Pulse train, produced by reverberation in PVC finally reaches lower electrode and produces pulses L2, L2′, L" and so on. Polarity is reversed because PZT is in expansion. Same train, when reflected from PZT-air interface, then reaches upper electrode and produces L3 pulse and so on.

A-scan of the voltage on the PZT element pulses labeled is presented in Fig. 16a, b, c (20 A pulse) and Fig. 17a, b (10 A 3–30 MHz chirp vs. 20 A 30 ns pulse). Spectra of L1 pulse (gate position is indicated by blue and red markers on A-scan) is presented in Fig. 16d, e, f (20 A pulse) and Fig. 17c, d (10 A 3–30 MHz chirp vs. 20 A 30 ns pulse).

In spectral plots black curve is for the received signal, while the blue curve is the expected AC response calculated using nominal duration of the excitation pulse (the one supplied to the input of laser driver). From the frequency domain response, it can be seen that the actual pulse duration is slightly shorter (the first spectral dip of the blue curve is at a slightly higher frequency than the black curve). This is caused by

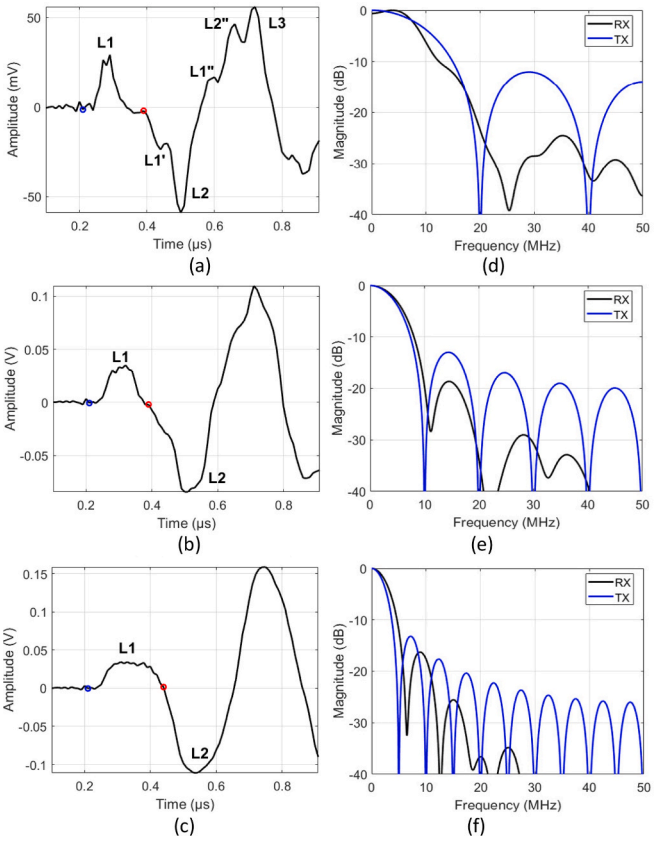

Fig. 16. Voltage registered on PZT element covered by black PVC tape when excited by pulse: 50 ns (a), 100 ns (b) and 200 ns (c) and corresponding spectra (d)-(f). Black: received signal, blue: excitation using nominal duration.

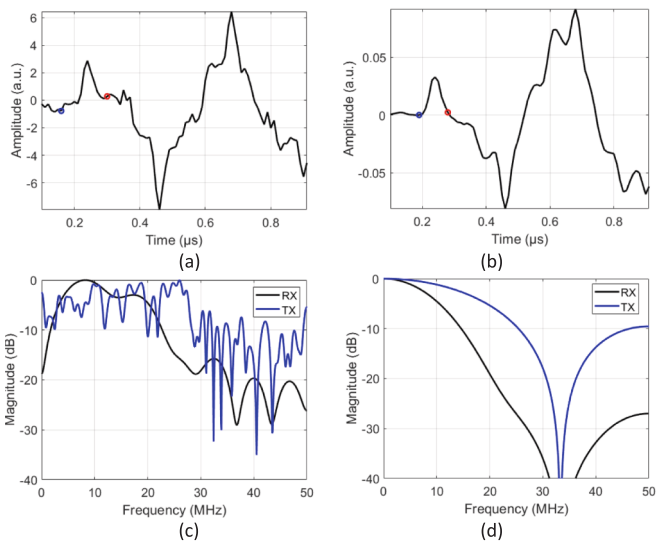

Fig. 17. Voltage on PZT element covered by black PVC tape when excited by 5–25 MHz 1 μs long chirp after PuC using matched filter (a) and excited by 30 ns pulse (b) and corresponding spectra (c),(d). Black: received signal, blue: excitation.

shortening of pulse in laser driver. It can be concluded that response duration follows the excitation pulse, only the response is slightly different from the one depicted in paint coating experiments (Fig. 7): pulse fronts are not that sharp. This can be expected since the PVC tape is soft and adhesion is through a sticky rubber (attenuative) that is applied on the PVC tape to create adhesion. Consequently, the AC response is sufficiently broadband but with some decay, caused by frequency-dependent attenuation in PVC tape and adhesive layer. Sensitivity is approximately 3 times higher than in case of thin paint coating and same for all durations: approximately 30 mV at 68 W laser power or approximately 440 μV/W.

Next experiment was aimed at evaluating the spatial resolution. The top electrode was covered by a black PVC tape only partially, so that the left half of the electrode does not receive the photoacoustic excitation. C-scan over 10x10 mm scan range of the L1 photoacoustic response is presented in Fig. 18. Data was acquired when the wider part of beam was oriented along the x-axis. Fig. 18a is for 50 ns pulse and Fig. 18b is for 5–30 MHz chirp excitation. PuC used inverse filter and the 0.2–25 MHz window.

It can be noted that spread spectrum excitation provides more details. Profile along the y-axis was taken for two cases: i) when wider part of the laser beam is along y axis (better resolution was expected along x axis) and ii) when wider part of the laser beam is along x axis (better resolution was expected along y axis). Obtained profile was processed

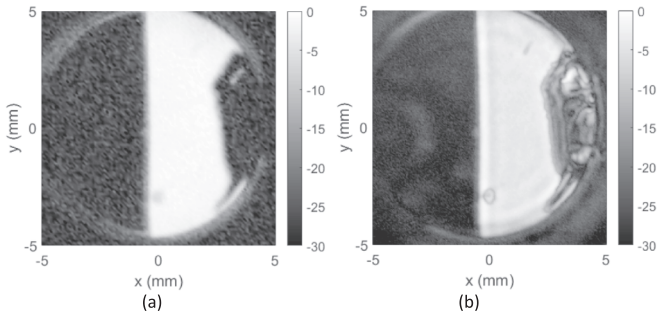

Fig. 18. C-scan of PZT element partly covered PVC tape when excited by 50 ns pulse (left) and 5–30 MHz chirp after PuC using inverse filter plus 0.2–25 MHz window (right) when wider part of the beam is along the x-axis. Grey scale is dB.

using knife edge beam profiling technique [64] to determine the obtained resolution. Resolution along the x-axis for 50 ns pulse excitation was 148 μm for case (i) and 203 μm for case (ii). Resolution along the x-axis for 5–30 MHz chirp excitation after inverse filter PuC plus 0.2–25 MHz window was 73 μm for case (i) and 83 μm for case (ii).

Next two experiments were aimed to evaluate the imaging performance of interface defects: i) a matching layer (black PVC tape) was loosely (to stimulate the development of local delaminations) attached to the PZT disk; ii) a human hair was placed at the interface between PZT and PVC tape. A scan over a 10x10 mm range was performed. The C-scan of the local delaminations when excited by 30 ns pulse and 5–30 MHz chirp after PuC is presented in Fig. 19. The C-scan of the hair defect between PZT and PVC tape when excited by a 30 ns pulse and 5–30 MHz chirp is presented in Fig. 20.

It can be noted that the 5–30 MHz chirp after PuC provides more details on interface defects than the 30 ns pulse, the broadest range coverage (5–30 MHz) produces better results compared to narrower ranges (2–20 MHz and 5–25 MHz were investigated, but images are not shown).

It is also worth noting that the pulse train structure in case of PVC tape as laser power absorbing material is different from paint coating case. The first pulse (L1) is the same, it is generated when the photoacoustic pulse hits the closest PZT electrode. The second pulse (L1′), appearing at 0.4 μs, is additional, it is a reverberation in PVC layer (refer Fig. 15 for explanation). It can be used to measure the acoustic thickness of PVC layer. Finally, the third pulse (L2), appearing at 0.45 μs, is generated from the interaction with the second electrode. It can be used to measure the acoustic thickness of PZT element.

Next experiment was aimed at measuring the acoustic thickness of the layers. A matching layer (black PVC tape) was attached to the PZT disk. A scan over the 10x10 mm range was performed. The A-scan of the photoacoustic response is presented in Fig. 21a, the black curve is the response when excited by the 30 ns pulse, while the magenta ("Fit") curve is the deconvolution result. Fig. 21b shows the individual pulses obtained from deconvolution, label number indicate the iteration at which pulse was extracted. It can be noted that largest pulses are extracted first. The correspondence to Fig. 15 is as follows: 1 is L2, 2 is L2", 3 is L1, 4 is L1', 5 is L1" and 6 is the artefact. L3 would have been extracted too if longer window was used for processing. The sum of all deconvolved reflections in Fig. 21a is constructed using all pulses shown in Fig. 21b.

The C-scans of the resonant frequency corresponding to the measured acoustic thickness (estimated from the ToF within the layer) are presented in Fig. 22 for matching layer λ/4 (a) and piezoelement λ/2 (b). The y-profile is presented in Fig. 23, blue curves are for λ/4 frequency of the matching layer, red curves-for λ/2 frequency of PZT.

It can be noted that the PZT disk has a uniform acoustic thickness, which matches its specified resonance frequency (2.25 MHz). Conversely, the matching layer thickness is not uniform and significantly deviates from the PZT resonance frequency (3.22–3.44 MHz versus the required 2.25 MHz).

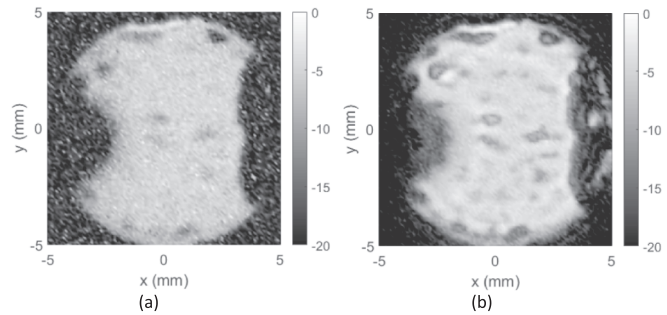

Fig. 19. C-scan of layer defects when excited by 30 ns pulse (top) and 5–30 MHz chirp after PuC (bottom). Grey scale is dB.

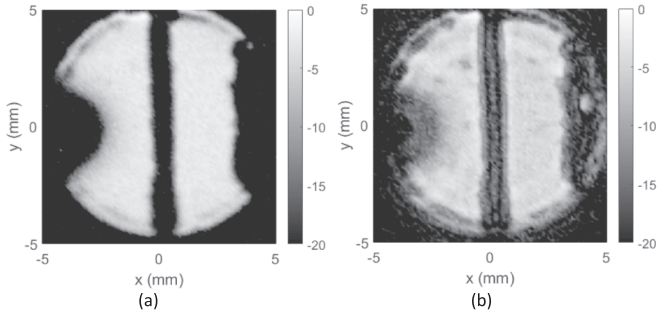

Fig. 20. C-scan of layer defects when excited by 30 ns pulse (top left), 5–30 MHz chirp (top right). Grey scale is dB.

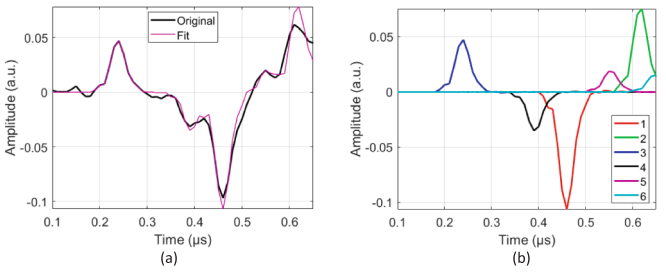

Fig. 21. A-scan of layer delamination defects when excited by the 30 ns pulse (top) and the 5–30 MHz chirp after PuC (bottom).

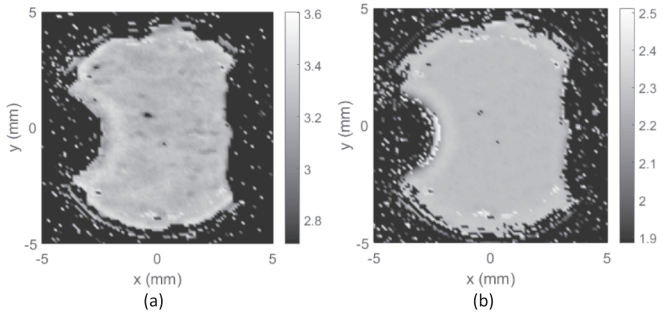

Fig. 22. C-scan of resonant frequency corresponding to measured acoustic thickness: for matching layer λ/4 (left) and piezoelement λ/2 (right). Grey scale is MHz.

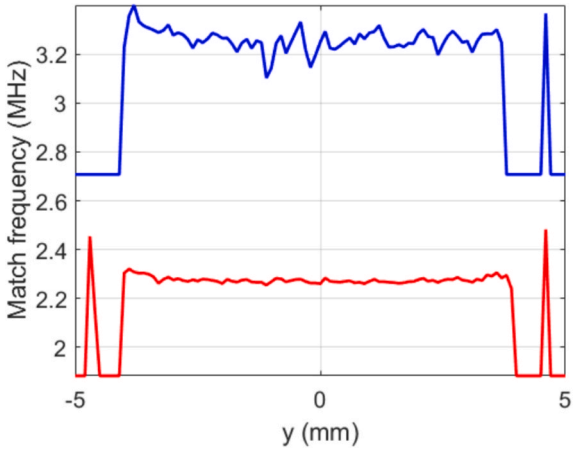

Fig. 23. Y-profile of resonant frequency corresponding to measured acoustic thickness: matching layer λ/4 (blue) and piezoelement λ/2 (red).

3.3. Air-coupled transducer made of vertical PVDF strips array

This experiment was aimed at evaluating the photoacoustic response of the transducer at various assembly stages (Fig. 24).

Four transducer configurations were investigated, representing different assembly stages: 1) only two PVDF strips suspended between two posts with 1.5 mm pitch, 2) same as (1), but backed 4 mm of UV-curable plastic on 1.5 mm FR4 plate, 3) same as (2) but covered by a membrane (100 μm thick paper or 23 μm thick water decal), and 4) a larger PVDF strips array with 200 μm pitch, backed and covered by water decal membrane. The excitation used a 500 ns, 20 A pulse. Two laser beam orientations were used: wider part of the beam along *x* axis (parallel to PVDF strip) and y axis (perpendicular to PVDF strip).

First set of experiments was aimed at evaluating the piezoelectric response of PVDF strip when excited by thermoelastic laser source. Laser beam was positioned over the edge of the PVDF strip in such way that laser beam center coincides with strip center. Wider part (103 μm) of the beam was along *x* axis (parallel to PVDF strip). In such case narrow (7 μm) part of the beam can completely penetrate into PVDF (thickness 50 μm).

No light absorbing coating was used in stage (1) since the edge of PVDF was directly exposed to laser radiation. Voltage on PVDF electrodes is presented in Fig. 25.

Information presented in Fig. 26 is aimed to explain the Fig. 25 results. This transducer operates the PVDF strips in d31 mode. Strips are cut in such way that d31 direction is upwards (Refer Fig. 2 and Fig. 25a). The upper edge of the strip is open, hence PVDF material is directly exposed to laser radiation. PVDF is almost transparent for 905 nm wavelength emitted by laser therefore narrow laser beam (7 μm) can propagate into PVDF (which 50 μm thick). Aluminum electrodes on both sides create the ideal waveguide (refer Fig. 25a), beam is trapped and fills the volume. Beam is focused at entrance point but spreads quickly at approximately 50° angle inside the strip so beam heating is over approximately 100 μm x 50 μm x 3000 μm volume.

FEM simulation was carried out to confirm the reaction shown in Fig. 25a. Excitation was simulated as a transient (rectangular 500 ns pulse with 10 ns fronts) heat source, covering whole PVDF strip thickness and exponentially decaying along strip height. At initial stage deformation is at the upper part of the strip (refer Fig. 26b). This extension is causing first pulse. Note a sharp, positive pulse at 0.75 μs, this is d33 mode reaction to expansion in thickness direction. Next negative pulse, appearing at 2 μs, corresponds to propagation at longitudinal velocity over 3 mm height. Heating the whole volume is also causing extension deformation along height. This deformation is causing damped oscillation which finally prevails (ringdown after first pulse). This direction is aligned with d31 mode at which this transducer operates [23]). Uniaxially stretched PVDF is used, therefore d_{31} coefficient is quite large. Sufficient voltage response can be expected even at low laser light absorption rate. Obtained voltage response on PVDF electrodes is quite similar to the experimentally obtained one (refer Fig. 25a). Other heat source distributions (e.g. uniform heating along the height) investigated in FEM simulation did not provide such similarity.

Voltage on PVDF electrodes obtained from stage (2) transducer is presented in Fig. 27. No light absorbing coating for the same reason:

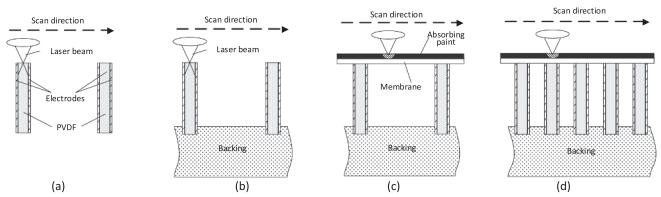

Fig. 24. Transducer configurations: two PVDF strips (a), two PVDF strips backed (b), two PVDF strips backed and covered by membrane (c) and fully assembled large and dense PVDF strips array (d).

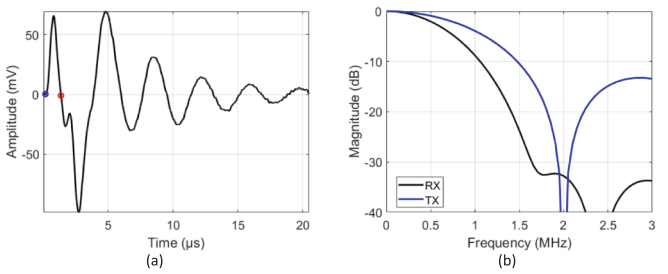

Fig. 25. Voltage on suspended vertical PVDF strip when excited by 500 ns pulse: time (a), and frequency (b) domain response.

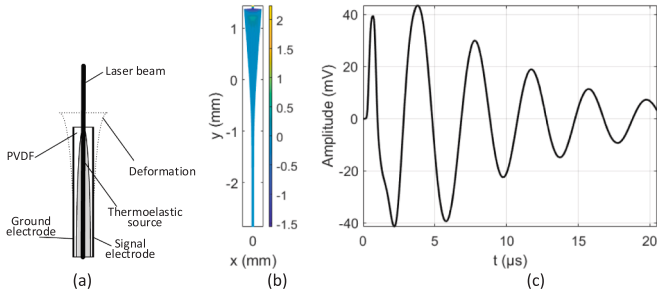

Fig. 26. Explanation of Fig. 25 results: topology view along length direction and deformation at initial excitation stage (a), comparison to deformations obtained (b) and A-scan of the signal obtained on PVDF electrodes (c) using FEM simulation.

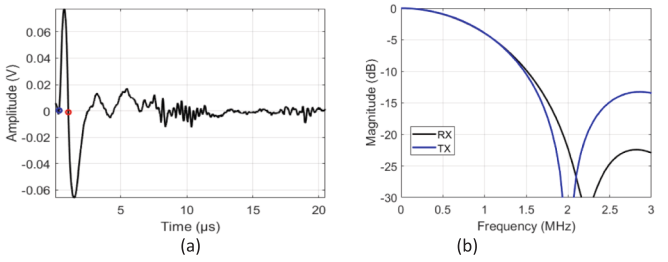

Fig. 27. Voltage on backed vertical PVDF strip when excited by 500 ns pulse: time (a) and frequency (b) domain response.

edge of PVDF was directly exposed to laser radiation. However, PVDF edge is covered by membrane in stage (3), therefore spray-coating with a black paint (BOKSC263206 type from Bostik SA, Colombes, France, 800 C°) was used in these experiments. Voltage on PVDF electrodes is presented in Fig. 28 (black curve in subplot (b): received signal after gating between the markers shown in subplot (a), blue curve: expected AC response according to code sequence used for excitation).

The narrow bandwidth response from the PVDF-based transducer is unusual: PVDF is considered a broadband material and is used for

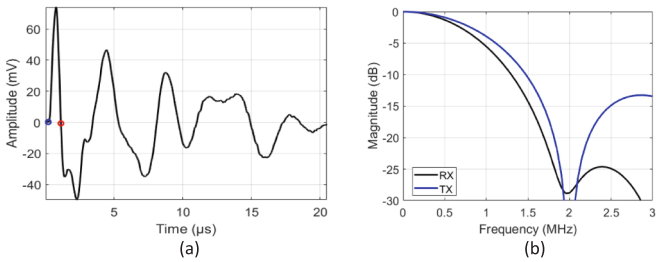

Fig. 28. Voltage on backed and membrane-attached vertical PVDF strip when excited by 500 ns pulse: time (a) and frequency (b) domain response.

transducers and wideband hydrophones manufacturing [56–58]. The reason is that ultrasonic transducers mostly use very small thickness (micrometers) PVDF sheets operating in the longitudinal d33 mode (pressure across the electrodes). In such case broadband response can obtained. Conversely, the transducer presented here uses PVDF in transversal d31 mode over 3 mm height because in this way a sensitivity higher than the d33 case can be obtained [23]. This mode is mainly used in energy harvesting and actuation [59,60]. The direction of actuation corresponds to the 3 mm width of the PVDF film here, therefore the response is narrowband, in exchange of a better matching to the air and higher sensitivity.

It can be noted that backing significantly reduces ringing. Such result has to be expected since this is precisely the purpose of backing: cancelling the reflection from the opposite edge [54,55]. Some ringing comes back with membrane attachment though, the oscillation is due to membrane flapping in this case.

Next experiment was aimed to evaluate the imaging capabilities of the vertical PVDF array transducer photoacoustic response at various assembly stages. The excitation used is a 500 ns, 20 A pulse. The C-scan of the assembly stage (1), when the PVDF strips (refer Fig. 2a or Fig. 24a) are suspended in air, is presented in Fig. 29. Same transducer was inspected using two different laser beam orientations: when wider part of the beam along *x* axis (parallel to PVDF strip) and rotated 90°.

When wider part of the beam is parallel to PVDF strip (Fig. 29a), better resolution was obtained in vertical direction. Blurring along vertical direction occurred in Fig. 29b because laser beam was perpendicular to PVDF strip.

The C-scan of the stage (2), backed by the absorbing material (Fig. 24b), is presented in Fig. 30.

Again, it can be concluded that the beam profile asymmetry can be useful in this investigation: the 7 μm resolution allows to distinguish the individual strips response along the y-axis, while the 100 μm resolution is sufficient along the x-axis. The loss of metallization (note the shorter upper strip) can be seen in Fig. 30, such defect cannot be located by visual inspection.

The inspection results of the next stages (refer Fig. 24c and Fig. 24d), i.e. when strips are backed and covered by the membrane, are presented in Fig. 31 and Fig. 32. Fig. 31 represents the Fig. 2a case, only two strips placed 1.5 mm apart, while Fig. 32 represents Fig. 2b case, where several strips are arranged with much denser, 200 μm pitch.

Again, loss of metallization (note the shorter upper strip in Fig. 31a) can be seen, no defects can be located in this case because membrane hides all transducer topology. A different kind of defect can be seen in Fig. 31b: the upper strip did not connect properly to the membrane, so its response is different from the lower one. It can be noted that the membrane application broadens the area where a thermoelastic response can be registered. For the case with the 1.5 mm spacing (Fig. 29-Fig. 31) between the strips, these sensitivity areas do not overlap, but once the complete assembly is done with 200 μm pitch, the areas overlap and a more uniform sensitivity is obtained (Fig. 31). Still, the individual responses from PVDF strips can be seen.

4. Conclusions

It was demonstrated that the photoacoustic excitation can be used for transducer sensitivity map production. A broadband photoacoustic response can be obtained if only the pressure signal registered on the

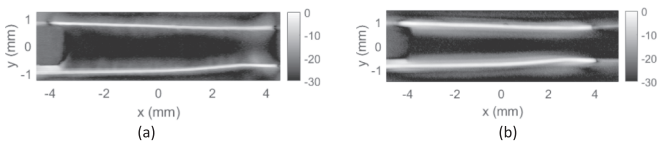

Fig. 29. C-scan of suspended PVDF strips: wider part of beam along x axis (a) and y axis (b). Grey scale is dB.

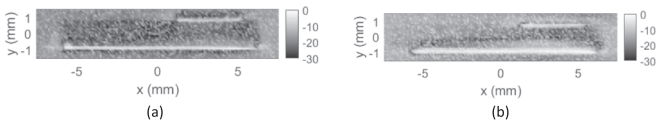

Fig. 30. C-scan of backed PVDF strips: wider part of beam along x axis (a) and y axis (b). Grey scale is dB.

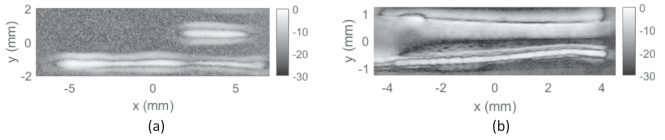

Fig. 31. C-scan of membrane type effects: paper (a) vs. water decal (b). Grey scale is dB.

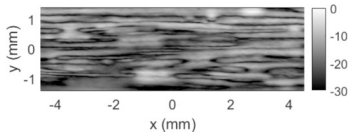

Fig. 32. C-scan of complete assembly of PVDF array transducer. Grey scale is dB.

front-facing piezoelement electrode is used. Attainable bandwidth was limited by the antialiasing filter to 0.3–30 MHz, which is much broader than expected bandwidth of undamped PZT disk with thickness resonance of 2 MHz. High (up to 30 MHz) upper frequency and small laser beam size (103x7 μm) allow to achieve high spatial resolution. Experimentally evaluated resolution for 50 ns pulse excitation was 148 μm or 203 μm depending on beam orientation. For 5–30 MHz chirp excitation after inverse filter PuC plus 0.2–25 MHz window resolution was 73 μm or 83 μm depending on beam orientation. The axial resolution is defined by bandwidth and in case of SS excitation and PuC it is down to 20 ns, which corresponds to 46 μm in PZT-5 ceramics or about 20 μm in PVDF or PVC.

It was demonstrated that: i) the implemented technique is a useful tool for transducer design inspection at various assembly stages, ii) it allows to locate transducer construction defects, and iii) it can be used to detect the delamination between piezoelements and matching layers. The use of spread-spectrum excitation, combined with pulse compression using inverse filtering further improves the performance of the proposed approach. The decomposition into pulse trains with separated components allows for measuring the acoustic thickness of the transducer layers, and to convert these values to the matching frequency of the layer or piezoelement.

Main application area of the proposed technique is ultrasonic transducer NDT at various design or manufacturing stages, inspection during operation. High spatial and temporal resolution allows to obtain the images which can be used to locate the electrode loss or matching layers delamination. With deconvolution applied, layers acoustic thickness can be measured as 2D map. Such map can be used to confirm whether every spot of the matching layer corresponds to the design frequency, evaluate the probe wear severity.

Technique can be expanded for laser ultrasound studies. Conventional way to measure laser ultrasound emission is by emission into water. Proposed allows to register the signal of thermoelastic source directly by PZT element, without water coupling. Response is broadband. Rayleigh, surface skimming longitudinal waves can also be registered and analyzed when part of electrode is removed from PZT element.

CRediT authorship contribution statement

Linas Svilainis: Writing – review & editing, Writing – original draft, Supervision, Software, Project administration, Methodology, Funding acquisition, Conceptualization. **Andrius Chaziachmetovas:** Writing – review & editing, Writing – original draft, Resources, Project administration, Investigation, Data curation, Conceptualization. **Luca De Marchi:** Writing – review & editing, Writing – original draft, Validation, Methodology, Formal analysis.

Declaration of competing interest

The authors declare that they have no known competing financial interests or personal relationships that could have appeared to influence the work reported in this paper.

Acknowledgments

This work was supported by the Research Council of Lithuania (LMTLT) under Grant S-MIP-23-133. Authors also acknowledge the help of dr. P. Kuzas and M. Varatinskas in experimental equipment preparation.

Data availability

Data will be made available on request.

References

[1] EN 12668-2:2010. Non-destructive testing - Characterization and verification of ultrasonic examination equipment - Part 2: Probes, (2010).
[2] EN 12668-3:2013. Non-destructive testing - Characterization and verification of ultrasonic examination equipment - Part 3: Combined equipment, (2013).
[3] IEC TS 62736:2023. Ultrasonics - Pulse-echo scanners - Simple methods for periodic testing to verify stability of an imaging system's elementary performance. Geneva.
[4] Electroacoustics - Measurement microphones - Part 3: Primary method for free-field calibration of laboratory standard microphones by the reciprocity technique, IEC 61094-3:2016, International Electrotechnical Commission, 2020.
[5] Underwater acoustics - Hydrophones - Calibration of hydrophones - Part 1: Procedures for free-field calibration of hydrophones, IEC 60565-1:2020, International Electrotechnical Commission, 2020.
[6] N.J. Dudley, S. Russell, B. Ward, P.R. Hoskins, BMUS guidelines for the regular quality assurance testing of ultrasound scanners by sonographers, Ultrasound 22 (1) (2014) 8–14, https://doi.org/10.1177/1742271X13511805.
[7] M. Martensson, et al., High incidence of defective ultrasound transducers in use in routine clinical practice, Eur. J. Echocardiogr. 10 (3) (2009) 389–394, https://doi.org/10.1093/ejechocard/jen295.
[8] R. Lorentsson, et al., Investigation of the impact of defective ultrasound transducers on clinical image quality in grayscale 2-D still images, Ultrasound Med. Biol. 49 (9) (2023) 2126–2133, https://doi.org/10.1016/j.ultrasmedbio.2023.06.004.
[9] O. Catalano, et al., Damage to ultrasound transducers, cables, and connectors. a pictorial guide to prevention, detection, and management, J. Ultrasound (2025), https://doi.org/10.1007/s40477-025-01041-8.
[10] T. Marhenke, S.J. Sanabria, B.R. Chintada, R. Furrer, J. Neuenschwander, O. Goksel, Acoustic field characterization of medical array transducers based on unfocused transmits and single-plane hydrophone measurements, Sensors 19 (4) (2019) 863, https://doi.org/10.3390/s19040863.
[11] Y.H. Yun, et al., The element by element acoustic power measurement of ultrasound array transducer for sonographic instrument, in 2006 World Congress On Medical Physics and Biomedical Engineering, 14 (14) (2007) 1609.
[12] A. Vuorenmaa, et al., Comparison of three quality assurance methods for clinical ultrasound devices, J. Med. Biol. Eng. 45 (2025) 147–155, https://doi.org/10.1007/s40846-025-00932-9.
[13] A. Lopez-Sanchez, L. Schmerr, Determination of an ultrasonic transducer's sensitivity and impedance in a pulse-echo setup, IEEE Trans. Ultrason. Ferroelectr. Freq. Control 53 (2006) 2101–2112, https://doi.org/10.1109/TUFFC.2006.150.
[14] D. Cowell, T. Carpenter, B. Fisher, S. Freear, In-situ measurement of transducer impedance using AFE active termination through analysis of ultrasound echoes, in 2017 IEEE International Ultrasonics Symposium, 1-4, doi: 10.1109/ULTSYM.2017.8092045.
[15] C. Silva, A. Alvarenga, R. Costa-Felix, Nondestructive testing ultrasonic immersion probe assessment and uncertainty evaluation according to EN 12668-2:2010, IEEE Trans. Ultrason. Ferroelectr. Freq. Control 59 (2012) 2338–2346, https://doi.org/10.1109/TUFFC.2012.2459.
[16] S.J. Sanabria, T. Marhenke, R. Furrer, J. Neuenschwander, Calculation of volumetric sound field of pulsed air-coupled ultrasound transducers based on

single-plane measurements, IEEE Trans. Ultrason. Ferroelect. Freq. Control 65 (1) (2018) 72–84, https://doi.org/10.1109/TUFFC.2017.2773619.
[17] T.E.G. Alvarez-Arenas, Acoustic impedance matching of piezoelectric transducers to the air, IEEE Trans. Ultrason. Ferroelectr. Freq. Control 51 (5) (2004) 624–633, https://doi.org/10.1109/TUFFC.2004.1320834.
[18] T. Gudra, K.J. Opielinski, Influence of acoustic impedance of multilayer acoustic systems on the transfer function of ultrasonic airborne transducers, Ultrasonics 40 (1–8) (2002) 457–463, https://doi.org/10.1016/S0041-624X(02)00159-2.
[19] L. Amoroso, et al., Novel nanocomposite materials for improving passive layers in air-coupled ultrasonic transducer applications, in: In IEEE International Ultrasonics Symposium (IUS), 2019, pp. 2608–2611, https://doi.org/10.1109/ultsym.2019.8925712.
[20] W. Ding, M. Bavencoffe, M. Lethiecq, Modeling and experimental characterization of bonding delamination in linear array ultrasonic transducer, in 2021 IEEE IEEE International Ultrasonics Symposium, 1-4, 2021, doi: 10.1109/IUS52206.2021.9593364.
[21] H. Tanaka, S. Machida, M. Nanri, Fabrication and evaluation of MUT-type acoustic metamaterial for impedance matching, IEEJ Trans. Electr. Electron. Eng. 19 (4) (2024) 586–594, https://doi.org/10.1002/tee.24038.
[22] A. Ba, et al., Soft porous silicone rubbers with ultra-low sound speeds in acoustic metamaterials, Sci. Rep. 7 (2017) 40106, https://doi.org/10.1038/srep40106.
[23] L. Svilainis, V. Eidukynas, L. De Marchi, A. Chaziachmetovas, Air-coupled ultrasound transduction improvement using vertical piezoelements' array, Sens. Actuators A Phys. 396 (2025) 117178, https://doi.org/10.1016/j.sna.2025.117178.
[24] J. Lu, J.F. Greenleaf, Evaluation of transducers with near-field scanning of their surfaces, in: IEEE International Ultrasonics Symposium (1994) 1163-1167, doi: 10.1109/ULTSYM.1994.401793.
[25] R. Lorentsson, N. Hosseini, J.O. Johansson, W. Rosenberg, B. Stenborg, L. G. Mansson, M. Bath, Method for automatic detection of defective ultrasound linear array transducers based on uniformity assessment of clinical images - a case study, J. Appl. Clin. Med. Phys. 19 (2) (2018) 265–274, https://doi.org/10.1002/acm2.12248.
[26] L. Zipser, H. Franke, Laser-scanning vibrometry for ultrasonic transducer development, Sens. Actuators A Phys. 110 (2004) 264–268, https://doi.org/10.1016/j.sna.2003.10.051.
[27] N.J. Dudley, Ultrasound probe acceptance testing using the in-air reverberation pattern, Ultrasound Med. Biol. 45 (6) (2019) 1475–1482, https://doi.org/10.1016/j.ultrasmedbio.2019.02.001.
[28] L. Svilainis, D. Kybartas, A. Aleksandrovas, T.E.G. Alvarez-Arenas, High frequency focused imaging for ultrasonic probe integrity inspection, NDT & E Int. 116 (2020) 102360, https://doi.org/10.1016/j.ndteint.2020.102360.
[29] L. Svilainis, A. Chaziachmetovas, D. Kybartas, and T. Gomez Alvarez-Arenas, Air-coupled ultrasonic probe integrity test using a focused transducer with similar frequency and limited aperture for contrast enhancement, Sensors 20 (24) (2020) 7196, doi: 10.3390/s20247196.
[30] M. Erfanzadeh, Q. Zhu, Photoacoustic imaging with low-cost sources: a review, Photoacoustics 14 (2019) 1–11, https://doi.org/10.1016/j.pacs.2019.01.004.
[31] S. Davies, C. Edwards, G. Taylor, S. Palmer, Laser-generated ultrasound: its properties, mechanisms and multifarious applications, J. Phys. D Appl. Phys. 26 (3) (1993) 329–348, https://doi.org/10.1088/0022-3727/26/3/001.
[32] M. Sanchez, D. Gallego, A.A. Oraevsky, H. Lamela, A laser ultrasound emitter based on high-power diode laser in overdrive operation mode for biomedical imaging applications, Ultrasonics 148 (2025) 107548, https://doi.org/10.1016/j.ultras.2024.107548.
[33] F. Gao, R. Kishor, X. Feng, S. Liu, R. Ding, R. Zhang, Y. Zheng, An analytical study of photoacoustic and thermoacoustic generation efficiency towards contrast agent and film design optimization, Photoacoustics 7 (2017) 1–11, https://doi.org/10.1016/j.pacs.2017.05.001.
[34] L. Svilainis, A. Aleksandrovas, Application of arbitrary pulse width and position trains for the correlation sidelobes reduction for narrowband transducers, Ultrasonics 53 (2013) 1344–1348, https://doi.org/10.1016/j.ultras.2013.04.001.
[35] L. Svilainis, A. Rodriguez-Martinez, A. Chaziachmetovas, A. Aleksandrovas, Ultrasound transmission spectral compensation using arbitrary position and width pulse sets, IEEE Trans. Instrum. Meas. 67 (8) (2018) 1778–1785, https://doi.org/10.1109/TIM.2018.2809838.
[36] M. Tayyib, L. Svilainis, SNR equalization in non-contact resonant ultrasound spectroscopy measurements, NDT E Int. 154 (2025) 103386, https://doi.org/10.1016/j.ndteint.2025.103386.
[37] L. Svilainis, A. Chaziachmetovas, V. Eidukynas, A. Aleksandrovas, M. Varatinskas, Compact laser driver for ultrasonic arbitrary position and width pulse sequences generation, IEEE Trans. Instrum. Meas. 70 (2021) 7006815, https://doi.org/10.1109/TIM.2021.3120144.
[38] D. Vella, Ultrasonic photoacoustic emitter of graphene-nanocomposites film on a flexible substrate, Photoacoustics 28 (2022) 100413, https://doi.org/10.1016/j.pacs.2022.100413.
[39] X. Hu, et al., Laser ultrasonic improvement and its application in defect detection based on the composite coating method, Appl. Opt. 61 (2022) 4145–4152, https://doi.org/10.1364/AO.454888.
[40] L. Svilainis, V. Dumbrava, S. Kitov, A. Aleksandrovas, P. Tervydis, D. Liaukonis, Electronics for ultrasonic imaging system, Elektron. Elektrotech. 20 (7) (2014) 51–56, https://doi.org/10.5755/j01.eee.20.7.8024.
[41] D. Hutchins, et al., Coded waveforms for optimised air-coupled ultrasonic nondestructive evaluation, Ultrasonics 54 (7) (2014) 1745–1759, https://doi.org/10.1016/j.ultras.2014.03.007.
[42] S. Laureti, et al., Delamination detection in polymeric ablative materials using pulse-compression thermography and air-coupled ultrasound, Sensors 19 (9) (2019) 2198, https://doi.org/10.3390/s19092198.
[43] L. Svilainis, M. Tayyib, Pulse compression for long spread spectrum signals application in air-coupled ultrasonic thickness resonance spectroscopy, IEEE Trans. Instrum. Meas. (2026), https://doi.org/10.1109/TIM.2026.3676189.
[44] L. Svilainis, K. Lukoseviciute, D. Liaukonis, Reiterative deconvolution: new technique for time of flight estimation errors reduction in case of close proximity of two reflections, Ultrasonics 76 (2017) 154–165, https://doi.org/10.1016/j.ultras.2017.01.003.
[45] R. Demirli, J. Saniie, Model-based estimation of ultrasonic echoes part i: analysis and algorithms, IEEE Trans. Ultrason. Ferroelect. Freq. Control 48 (3) (2001) 787–802, https://doi.org/10.1109/58.920713.
[46] K.F. Kaaresen, E. Bolviken, Blind deconvolution of ultrasonic traces accounting for pulse variance, IEEE Trans. Ultrason. Ferroelect. Freq. Control 46 (3) (1999) 564–573, https://doi.org/10.1109/58.764843.
[47] G.M. Zhang, C.Z. Zhang, D.M. Harvey, Sparse signal representation and its applications in ultrasonic NDE, Ultrasonics 52 (3) (2012) 351–363, https://doi.org/10.1016/j.ultras.2011.10.001.
[48] X.G. Li, Q.H. Qin, X. Wang, Y.H. Miao, Ambient noise-based passive reconstruction of dispersion curve in a thin-plate with complex boundary interferences using sparse learning, Mech. Syst. Signal Proc. 239 (2025) 113271, https://doi.org/10.1016/j.ymssp.2025.113271.
[49] Y. Lu, R. Demirli, G. Cardoso, J. Saniie, A successive parameter estimation algorithm for chirplet signal decomposition, IEEE Trans. Ultrason. Ferroelect. Freq. Control 53 (11) (2006) 2121–2131, https://doi.org/10.1109/TUFFC.2006.152.
[50] I. Barrodale, C.A. Zala, N.R. Chapman, Comparison of the L1 and L2 norms applied to one-at-a-time spike extraction from seismic traces, Geophysics 49 (11) (1984) 2048–2052.
[51] S.G. Mallat, Z. Zhang, Matching pursuits with time-frequency dictionaries, IEEE Trans. Signal Processing 41 (1993) 3397–3415, https://doi.org/10.1109/78.258082.
[52] T. Misaridis, J.A. Jensen, Use of modulated excitation signals in medical ultrasound. Part II: design and performance for medical imaging applications IEEE Trans, Ultrason. Ferroelect. Freq. Control 52 (2005) 192–207, https://doi.org/10.1109/TUFFC.2005.1406546.
[53] C. Challinor, F. Cegla, Pulse compression with and without matched filtering: why codes beat chirps, NDT & E Int. 147 (2024) 103180, https://doi.org/10.1016/j.ndteint.2024.103180.
[54] H. Kim, et al., High-attenuation backing layer for miniaturized ultrasound imaging transducer, IEEE Trans. Ultrason. Ferroelect. Freq. Control 69 (6) (2022) 1960–1969, https://doi.org/10.1109/TUFFC.2022.3164451.
[55] C.X.Hou et al., Optimized backing layers design for high frequency broad bandwidth ultrasonic transducer, IEEE Trans. Biomed. Eng. 69 (1) (2022) 475-481, doi: 10.1109/TBME.2021.3098567.
[56] Y.H. Liu, et al., Highly sensitive miniature needle PVDF-TrFE ultrasound sensor for optoacoustic microscopy, Adv. Photon. Nexus 2 (5) (2023), https://doi.org/10.1117/1.APN.2.5.056006.
[57] J. Chen, et al., Quasi-spherical PVDF ultrasonic transducer with double-cylindrical PVDF structure, IEEE Sens. J. 20 (1) (2020) 113–120, https://doi.org/10.1109/JSEN.2019.2941980.
[58] C.V. Vishnu, et al., Underwater acoustic performance of a planar PVDF hydrophone: simulation and experimental validation, Measurement 245 (2025) 116597, https://doi.org/10.1016/j.measurement.2024.116597.
[59] A. Megdich, et al., Enhanced piezoelectric performance of PVDF/MWCNTs energy harvester through a 3D-printed multimodal auxetic structure for smart security systems, Mater. Today Sustain. 27 (2024) 100847, https://doi.org/10.1016/j.mtsust.2024.100847.
[60] K.N. Wang, et al., Adaptive shell spherical reflector actuated with PVDF-TrFE thin film strain actuators, Actuators 10 (1) (2021) 7, https://doi.org/10.3390/act10010007.
[61] T. Kurzynowski, E. Chlebus, B. Kuźnicka, J. Reiner Parameters in selective laser melting for processing metallic powders, in: Proceedings of SPIE LASE, Vol. 8239, 2012, 823914, doi: 10.1117/12.907292.
[62] N. Ahbab, S. Naz, T.-B. Xu, S.A. Zhang, Comprehensive review of piezoelectric PVDF polymer fabrications and characteristics, Micromachines 16 (2025) 386, https://doi.org/10.3390/mi16040386.
[63] P. Burrascano, S. Laureti, L. Senni, M. Ricci, Pulse compression in nondestructive testing applications: reduction of near sidelobes exploiting reactance transformation, IEEE Trans. Circuits Syst. i: Regul. Pap. 66 (5) (2019) 1886–1896, https://doi.org/10.1109/TCSI.2018.2862868.
[64] M.A.C. de Araújo, E. de Lima, D.P. Pereira, P.C. de Oliveira, Measurement of Gaussian laser beam radius using the knife-edge technique: improvement on data analysis, Appl. Optics 48 (2) (2009) 393–396, https://doi.org/10.1364/AO.48.000393.